Submitted to Engineering Failure Analysis

Comparison of hydrogen diffusion properties and hydrogen-induced ductility loss of additively and conventionally manufactured 17-4PH stainless steel

Junichiro Yamabe,[a,b*] Soma Kato,[a] Kazuyuki Morishita,[c] and Kentaro Wada[d]

[a] Department of Mechanical Engineering, Fukuoka University, 8-19-1 Nanakuma, Jonan-ku, Fukuoka-shi, Fukuoka-shi, Fukuoka 814-0180, Japan

[b] Research Institute of Materials Science and Technology, Fukuoka University, 8-19-1 Nanakuma, Jonan-ku, Fukuoka-shi, Fukuoka 814-0180, Japan

[c] Industrial Technology Center of Fukui Prefecture, 10 Aza-Kitainada, 61 Kawai Washizuka-cho, Fukui-shi, Fukui 910-0102, Japan

[d] National Institute for Materials Science (NIMS), 1-2-1 Sengen, Tsukuba-shi, Ibaraki 305-0047, Japan

*Corresponding author, E-mail: jyamabe@fukuoka-u.ac.jp

Abstract

Hydrogen diffusion properties and hydrogen-induced ductility loss of an as-built 17-4PH stainless steel fabricated by the additive manufacturing (AM) process were investigated using hydrogen-charged specimens exposed to high-pressure gaseous hydrogen and the results were compared with those of a conventionally manufactured 17-4PH steel under solution-treated (ST) and precipitation-hardened (PH) conditions. Peak-aged (H900) and over-aged (H1150) steels were prepared for the PH conditions. The austenite fraction of the additively manufactured materials was at most three times higher than that of the ST material. Except for the H900 material, the saturated hydrogen content of both the additively manufactured and conventional materials was dominated by the austenite in the materials. Hydrogen trapping by Cu precipitation, not the austenite, was considered to be mainly responsible for the saturated hydrogen content of the H900 material. The hydrogen diffusivity for both the additively manufactured and ST materials also decreased with higher austenite fractions. In the uncharged situation, the reduction in area (RA) of the additively manufactured material was larger than that of the conventional materials. In the hydrogen-charged situation, the additively manufactured material had a lower relative reduction in area (RRA) compared to that of the ST material, although their tested tensile strengths were similar. The hydrogen-charged additively manufactured and ST materials had quasi-cleavage (QC) surfaces. Voids elongated in the direction perpendicular to the loading direction, which corresponded to the QC facets, were observed from the longitudinal cross sections of both the additively manufactured and ST materials, suggesting the contribution of hydrogen–dislocation interactions.

Keywords:
Hydrogen embrittlement; 17-4 PH steel; Additive manufacturing; Slow strain-rate tensile testing; Retained austenite

1. Introduction

Global warming, which is known to be caused by the emission of carbon dioxide (CO_2), is an urgent problem to be solved. Among the various attempts being made throughout the world to reduce CO_2 emissions is a promising technology that involves the utilization of hydrogen energy. Because the ductility of many metals is degraded by hydrogen, the mechanisms of hydrogen embrittlement (HE) need to be understood, thereby enabling scientists and engineers to ensure the safety and durability of hydrogen-containing components on the basis of scientific evidence. Many studies on HE-related problems of practical importance have been conducted thus far [1–16], enabling reasonable materials-selection [17,18] and strength-design [19–21] methods to be proposed in consideration of HE.

Recently, the utilization of liquid hydrogen with an energy density higher than that of high-pressure hydrogen gas has been actively investigated. The increased utilization of high-pressure hydrogen has increased the necessity for large components with complicated shapes. In the case of liquid hydrogen boil-off, it is necessary to collect data regarding HE in a wide temperature range. In addition, because the application of conventional wrought and rolled alloys in such components often leads to high machining costs, new technologies are needed to create such components at lower cost. For example, austenitic stainless steels are considered difficult-to-cut materials; therefore, creating large components with complicated shapes using wrought and rolled steels without increasing machining costs is difficult. Therefore, if cast and additively manufactured alloys are used for these components, they can be widely applied because a substantial reduction of the machining cost is expected. Additively manufactured alloys have more manufacturing parameters than cast alloys, and the additive manufacturing (AM) process has an advantage in that high-strength alloys with small defects can be developed under optimized manufacturing conditions.

The AM technique is a process of joining materials layer upon layer, which is different from subtractive manufacturing methodologies. In the AM of metals, selective laser melting (SLM), direct energy deposition (DED), fused deposition modeling (FDM), and the binder jet (BJT) process are often used. The advantages of these methods include enabling the creation of three-dimensional components with complicated shapes that cannot be created by other machining processes. The methods can also express internal structures as well as at surfaces and create lattice structures and functional gradient materials. In each selected method, the manufacturing parameters must be optimized since they significantly affect the quality of the additively manufactured components [22]. At present, the parameters are mostly controlled to minimize the porosity ratio [23]. In its early days,

the AM process was mainly used for product prototypes; however, reduction of the manufacturing cost and improvements of the quality and throughput have expanded the application of the AM process to practical products, mainly in factories that produce small quantities of many different products. Accompanied by the expansion of the AM process, the strength properties of additively manufactured materials have become important. The strength properties of stainless steels [24–28], titanium alloys [29,30], nickel alloys [31], and aluminum alloys [32] fabricated by AM have been evaluated in past studies. The effect of the unique AM-induced microstructures on the strength properties has also been evaluated and is reported to improve the strength–ductility balance [27,28,33]. In addition, although numerous studies have covered the effect of hydrogen on the tensile properties of additively manufactured alloys, fundamental knowledge still needs to be accumulated.

The present study deals with a precipitation-hardened martensitic stainless steel, 17-4PH, because the conventional 17-4PH steel is known to be severely embrittled by hydrogen [38] and a review paper of additively manufactured 17-4PH steel has been published [39]. According to the existing literature, additively manufactured steel tends to have a higher tensile strength and lower ductility than conventional steel. The elevated tensile strength is attributed to fine microstructures formed via the rapid melting and solidification process, and the reduced ductility is attributed to porosity. On the other hand, in some cases, a large amount of metastable phases of retained austenite exist in the additively manufactured steel in relation to the mechanical stability of austenite phases due to the residual thermal stress during the manufacturing process and the transformation-induced plasticity (TRIP) effect of these metastable retained austenite phases improves the ductility of the additively manufactured steel [39–41]. Although there are various reports on the tensile properties and microstructures of 17-4PH steel with the AM process in the absence of hydrogen, research on the HE of the steel is limited [42]. Thus, the present study prepared an as-built additively manufactured 17-4PH steel without any heat treatment as the first step to determining the HE of additively manufactured materials. The hydrogen-induced ductility loss of the steel, which provides fundamental data for discussing the hydrogen compatibility of materials, were determined and the similarity and difference in the experimental results between the additively manufactured and conventional materials were compared. In addition, because this study evaluated the degree of HE with hydrogen-charged specimens, the saturated hydrogen concentrations in the materials need to be confirmed by hydrogen charging and negligible hydrogen desorption during tensile tests. Thus, these hydrogen diffusion properties were also determined.

2. Materials and methods

2.1 Additively manufactured material

The powder material was Matsuura Stainless 630, mainly composed of 16.3 Cr, 4.0 Ni, and 4.0 Cu in wt.%, with the balance being Fe. This material corresponds to 17-4PH steel. The powder size

ranged from 10 to 45 μm and the average size was 24 μm. A metal 3D printer (Lumex Avance-25, Matsuura Machinery Corp.) was used for the process and the additively manufactured material was fabricated via the SLM method. The AM conditions were as follows: laser power 200 W, spot size 0.15 mm, scanning rate 800 mm/s, hatching pitch 0.08 mm, and laminating pitch 0.05 mm.

Figure 1 depicts the geometry of the raw materials and the laminating directions. On a base plate of 130×130 mm, raw materials with a longitudinal direction corresponding to the *x* direction (AM-x) and *z* direction (AM-z) were manufactured. Two raw materials of AM-x and six raw materials of AM-z were manufactured from one plate. The raw materials were tested under as-built conditions without any heat treatment as the first step to accumulating fundamental data on the additively manufactured material. The densities of AM-x and AM-z were 7.75 and 7.71 g/cm^3, respectively, which were slightly lower than that of the conventional 17-4PH steel (7.81 g/cm^3). The density was determined via the Archimedes method.

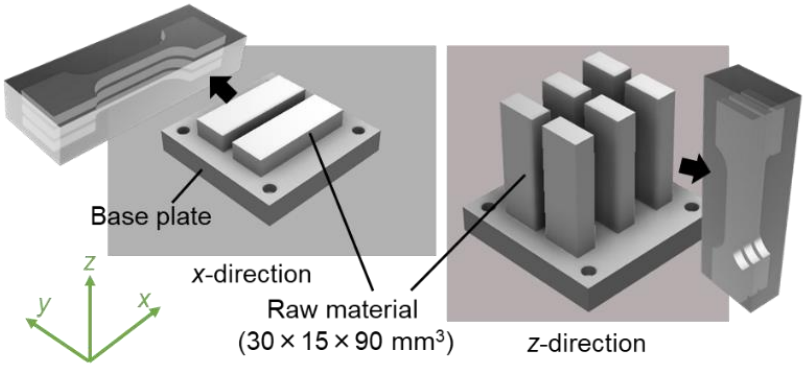

Fig. 1 Laminating directions and raw AM materials.

2.2 Conventional material

Table 1 shows the chemical compositions of conventional 17-4PH steels for comparison with the additively manufactured material. **Table 2** shows the heat treatment conditions. Two conventional materials were used in this study. One of them was a round-bar and the other was a plate, which were referred to as SUS630-R and SUS630-P, respectively. The chemical compositions of the materials were similar and satisfied the Japanese Industrial Standards (JIS) requirements. Solution-treated (ST) and precipitation-hardened (PH) materials were prepared. Due to preparation difficulties using the stock of conventional materials, the ST and PH materials were manufactured from SUS630-R and SUS630-P, respectively. The ST material was referred to as ST-R. In the PH material, peak-aged and over-aged materials were prepared, referred to as H900-P and H1150-P, respectively. H900-P and H1150-P were used only for microstructural and hydrogen analyses. A slight difference in the chemical compositions between the additively manufactured and conventional steels was observed. Although a slight difference in Cu contents can affect the distribution of Cu precipitates contributing

to precipitation hardening, this study used an as-built additively manufactured 17-4PH steel without any heat treatment; therefore, the slight difference in the chemical composition is considered to hardly affect the experimental results.

Table 1 Chemical composition of conventional materials [wt.%]

Material	C	Si	Mn	P	S	Cu	Ni	Cr	Nb
SUS630-R	0.04	0.31	0.87	0.034	0.004	3.3	4.24	15.57	0.34
SUS630-P	0.04	0.34	0.86	0.034	0.006	3.3	4.26	15.65	0.24
JIS requirements	≤ 0.07	≤ 1	≤ 1	≤ 0.040	≤ 0.030	3–5	3–5	15–17.5	0.15–0.45

Table 2 Heat-treatment conditions of conventional materials

Symbol	Solution treatment	Aging treatment
ST-R	1040°C for 1 h, followed by water quenching with salt bath	–
H900-P		480°C for 2 h, followed by air cooling with salt bath
H1150-P		620°C for 4 h, followed by air cooling with salt bath

2.3 Specimens

Figure 2 shows the shape and dimensions of the slow strain-rate tensile (SSRT) specimen. A rectangular specimen with a square cross section of 4 mm × 4 mm and a gauge length of 30 mm was used. Three rectangular specimens were machined from one raw additively manufactured material via electron discharge machining (EDM). After the EDM, the specimen surface was polished by using emery papers from #180 to #2000. A cubic-like specimen with a length of one side of 5 mm was used for measuring the hydrogen content, whereas a cylindrical specimen with a diameter of 8 mm and a

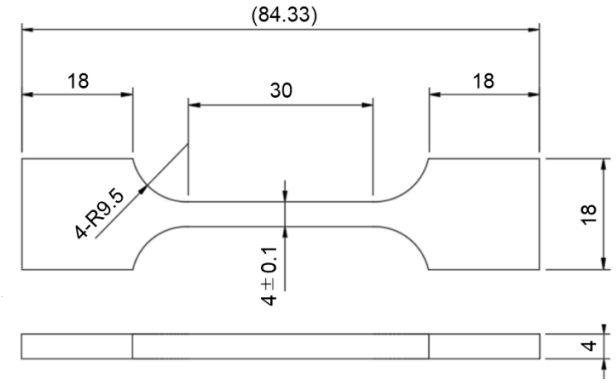

Fig. 2 Shape and dimensions (in mm) of SSRT specimen.

length of 8 mm was used for measuring the hydrogen diffusivity. The cylindrical specimen was sampled to satisfy that the length direction of the cylindrical specimen was parallel to the longitudinal direction of the raw material. As with the SSRT specimen, the surfaces of these specimens were finished by polishing with emery papers from #180 to #2000. The SSRT test of ST-R was performed using a round-bar specimen with a diameter of 6 mm and a gauge length of 30 mm, which was the same geometry as that used in our previous study [38].

2.4 Microstructural analyses

The existence of fine microstructures and a higher fraction of metastable retained austenite phases have been reported in additively manufactured 17-4PH steels [39,41]. The microstructures were analyzed by means of scanning electron microscopy–electron backscattered diffraction (SEM–EBSD; SEM: JSM-7001F, JEOL; EBSD: OIM, AMETEK) under an acceleration voltage of 20 kV and a step size of 0.25 μm. In addition, it was predicted that the metastable austenite phases significantly affect the HE and hydrogen diffusion properties [14]. Thus, the fraction of austenite phases was quantified via X-ray diffraction (XRD; RINT-RAPID II, Rigaku) with a cobalt tube at 40 kV and 30 mA. The X-ray detector was a two-dimensional imaging plate and the diameter of a collimator was 300 μm. To reduce the effect of the crystal orientation, angles of φ and ω were rotated at 1°/s and 2°/s (25°–35°) during 30 min, respectively. The additively manufactured materials (AM-x and AM-z) were measured twice and the austenite fractions were determined by Rietveld analysis.

2.5 Hydrogen charging and measurements of hydrogen content and diffusivity

Some of the specimens were charged in hydrogen gas at 100 MPa and 270°C for 200 h. The charging conditions were selected to obtain saturated hydrogen concentrations in all of the specimens. The hydrogen diffusivity of the conventional 17-4PH steel at 270°C is reported to be 5×10^{-10} m^2/s at minimum [38]. The hydrogen diffusivity and the charging time are denoted by D and t, respectively. When the value of $\sqrt{Dt}$ is larger than the half length of a specimen, the specimen approximately reaches a uniform hydrogen distribution. When D was 5×10^{-10} m^2/s and t was 200 h, the value of $\sqrt{Dt}$ was 19 mm, which is higher than the half length of all the specimens used in this study, suggesting that the hydrogen concentration of all the specimens reached the saturated condition by the present hydrogen charging. The hydrogen analysis was conducted by means of gas chromatography–mass spectroscopy (GC–MS; GTF-20A, J-SCIENCE). The saturated hydrogen content was determined by measurement under a rising temperature, otherwise known as thermal desorption analysis (TDA). The heating rate was 100°C/h and the evaluated temperature ranged from room temperature up to 600°C. The hydrogen diffusivity was determined by fitting the solution of a diffusion equation to the residual hydrogen content, C_{HR}, measured at various constant temperatures, and is called the desorption method [43–45].

$$C_{\mathrm{HR}} = \frac{32}{\pi^2} \cdot A \cdot \left\{ \sum_{n=0}^{\infty} \frac{\exp\left[-\frac{(2n+1)^2 \pi^2 D t_{\mathrm{R}}}{z^2} \right]}{(2n+1)^2} \right\} \cdot \left\{ \sum_{m=1}^{\infty} \frac{\exp\left[-\frac{D \beta_m^2 t_{\mathrm{R}}}{r^2} \right]}{\beta_m^2} \right\} \quad (1)$$

where A is the value related to the saturated hydrogen content, D is the hydrogen diffusivity, r is the specimen radius, z is the specimen thickness, β_m is the root of the zero-order Bessel function, and t_{R} is the holding time in GC–MS. **Figure 3** illustrates an example of the fitting of Eq. (1) to C_{HR} via the least-squares method. Since the experimental data included the hydrogen content during a rapid heating process before reaching a constant temperature, the fitting was performed by excluding the data during the process. Thus, the strict solution of Eq. (1) is not A, but is instead the saturated hydrogen content, C_{HS}; however, the determined A value is not necessarily consistent with the value of C_{HS}.

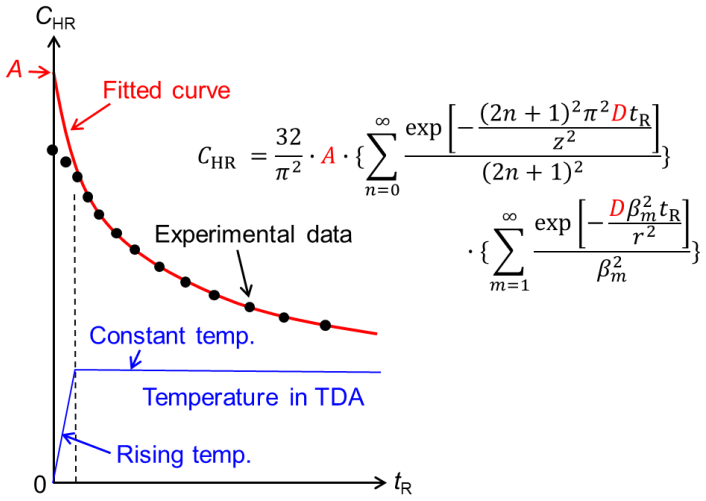

Fig. 3 Schematic illustration of hydrogen diffusivity determination via the desorption method.

2.6 SSRT tests and observation of fracture morphologies

SSRT tests of uncharged and H-charged specimens were performed with a tensile tester (Autograph AG-X, Shimadzu) at an initial strain rate of 5×10^{-5} s^{-1} in air at room temperature. After the SSRT tests, fractures and outer surfaces of the specimens were observed via SEM (SU1510, Hitachi). Longitudinal cross sections were cut from some of the specimens, after which void formation was observed by optical microscopy.

3. Results

3.1 Microstructures analyzed by optical microscopy and SEM–EBSD

Figure 4 shows the optical microscopy images of AM-x and AM-z. According to the images, only a few porosities were detected and their maximum size was ~15 μm. The porosity ratio, *d*, can be calculated using the density of the additively manufactured and conventional steels as follows:

$$d = 1 - \frac{\rho_{\mathrm{AM}}}{\rho_{\mathrm{C}}} \qquad (2)$$

where ρ_{AM} is the density of the additively manufactured material and ρ_{C} is the density of the conventional material. Because the densities of AM-x, AM-z, and the conventional material were 7.75, 7.71, and 7.81 g/cm^2, respectively, the porosity ratios of AM-x and AM-z were calculated to be 0.0078 (0.78%) and 0.013 (1.3%), respectively.

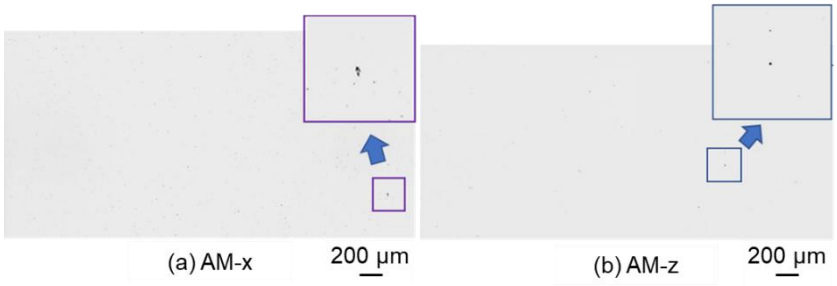

Fig. 4(a) Optical microscope images of AM-x and AM-z.

Figure 5 shows the inverse pole figure (IPF) and phase maps of AM-x, AM-z, ST-R, and H1150-P. The average grain sizes and corresponding standard deviations are shown in the figure. It is known that the additively manufactured material has finer microstructures than the conventional materials [39]. Although the microstructural morphology of AM-x and AM-z was not dependent on the lamination direction, these average grain sizes were smaller than those of ST-R and H1150-P, demonstrating that the microstructures of the additively manufactured materials were finer than those of the conventional ones as well as those reported in the literature. Regarding austenite phases, whereas the austenite fractions determined from the phase maps were nearly zero for AM-x and AM-z, those of ST-R and H1150P determined from the phase maps were 5.4% and 15.4%, respectively. These values will be compared with those determined by XRD.

3.2 Austenitic content determined by XRD

Figure 5 shows the X-ray diffraction patterns of the additively manufactured (AM-x, AM-z) and conventional (ST-R, H900-P, H1150-P) materials. Austenite fractions of the materials are also provided in the figure. There was no substantial difference in the austenite fractions between ST-R and H900-R, which was around 7%. Compared to this, an austenite fraction of more than 20% was detected

from H1150-P. The austenite fractions of ST-R and H1150-P determined from the phase maps were 5.4% and 15.4%, which are slightly lower than those determined by XRD. The large austenite fraction of H1150-P is mainly attributed to the reversed austenite phases produced by the PH treatment [46].

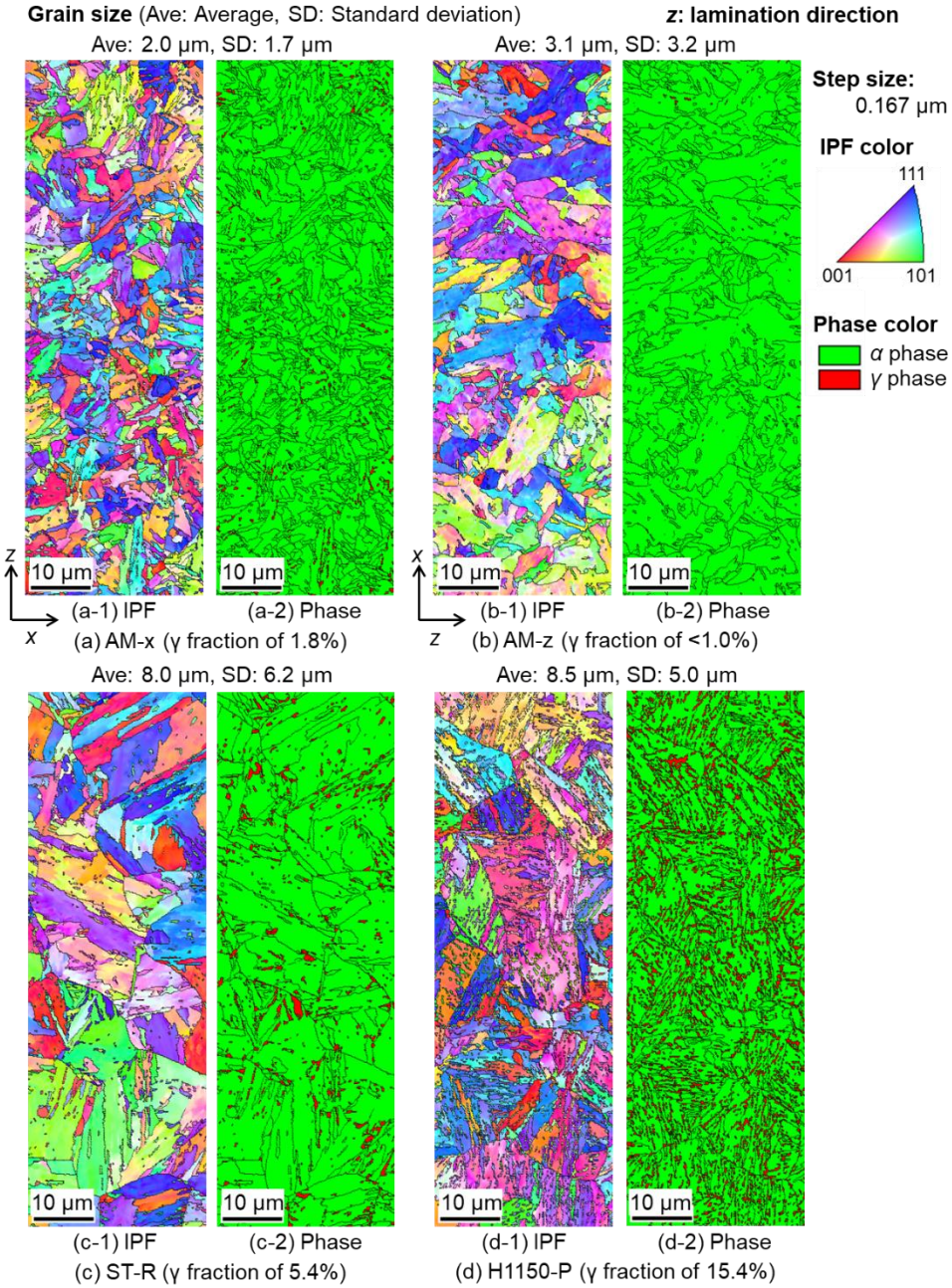

Fig. 5 Inverse pole figure (IPF) and phase maps of additively manufactured and conventional materials analyzed by SEM/EBSD.

On the other hand, an austenite fraction of around 27% was detected from AM-x, which was higher than that of H1150-P. Regarding AM-z, there was a larger scatter in the austenite fraction and

its values ranged from 10.2% to 20.8%. It has been reported that additively manufactured materials have a high fraction of metastable residual austenite phases in relation to the residual thermal stress during the manufacturing process and its fraction varies according to the AM conditions [39,41]. The high fraction of austenite phases in AM-x and the difference in the austenite fraction between AM-x and AM-z are potentially explained by this mechanism, although the reason for the larger scatter of the austenite fraction of AM-z has not been clarified. In addition, the austenite fractions of AM-x and AM-z determined by SEM-EBSD were nearly zero—considerably lower than those determined by XRD. This discrepancy is attributed to a problem related to step size, suggesting that the austenite phases of the additively manufactured materials were finer than those of the conventional ones. Therefore, further studies with a smaller step size are needed to identify the distribution and morphology of the austenite phases of the additively manufactured materials.

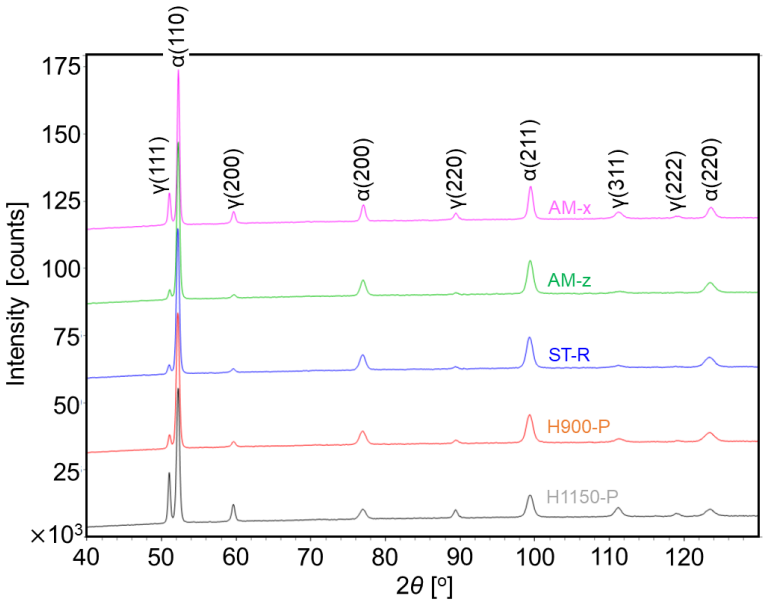

Fraction of γ phases [%]	
AM-x	26.5 ~ 27.5
AM-z	10.2 ~ 20.8
ST-R	7.5
H900-P	6.9
H1150-P	23.2

Fig. 6 X-ray diffraction patterns and austenite fractions of additively manufactured and conventional materials determined by XRD.

3.3 Hydrogen uptake

Table 3 summarizes the hydrogen content, C_H, of the additively manufactured and conventional materials after hydrogen charging at 100 MPa and 270°C for 200 h. The hydrogen content corresponds to the saturated hydrogen content, C_{HS}, at 100 MPa and 270°C. Measurements were done twice for AM-x and AM-z. The values of C_{HS} for AM-z showed a large scatter as well as the austenite fractions. This is because the saturated hydrogen content of AM-z was dominated by the austenite fraction. The C_{HS} values differed between the materials and its descending order by content was AM-x > H1150-P > H900-P > AM-z > ST-R.

Table 3 Saturated H content of additively manufactured and conventional materials.

Symbol	C_{HS} [wt.ppm]
AM-x	33.7– 33.9
AM-z	12.7–17.5
ST-R	2.4
H900-P	17.4
H1150-P	24.8

Figure 7 shows the relationship between the saturated hydrogen content and the austenite fractions. The average values of the saturated hydrogen content and austenite fractions were used for AM-x and AM-z. Except for H900-P, the saturated hydrogen content of the additively manufactured and conventional materials was dominated by the austenite contained in the materials. Since the saturated hydrogen content of austenite is approximately two orders of magnitude larger than that of martensite, the difference in the saturated hydrogen content between the materials, except for H900-P, is mainly attributed to their different austenite fractions. As for H900-P, there is a significant hydrogen trapping effect of fine Cu precipitates formed by the PH treatment [38]. This hydrogen trapping effect is considered to be responsible for H900-P having a hydrogen content around eight times larger than that of ST-R, despite their similar austenite fractions.

3.4 Hydrogen diffusivity

The hydrogen diffusivity of the additively manufactured materials was compared with that of the conventional materials. **Figure 8** shows the Arrhenius plots of the additively manufactured materials, together with literature data of conventional materials for 17-4PH (ST and PH) and 300-series austenitic stainless steels [12,38]. The ST in the literature is the same as ST-R. The solid lines in the figure are approximations obtained by fitting Eq. (3) to the experimental data with the least-squares method:

$$D = D_0 \exp\left(-\frac{E_D}{RT}\right) \qquad (3)$$

where D_0 is a constant that is not dependent on the temperature, E_D is the activation energy of hydrogen diffusion, R is the gas constant, and T is the absolute temperature. The E_D values of AM-z and ST-R were nearly equal, and slightly higher than that of AM-x. The diffusivity of AM-z was higher than that of AM-x. These values were one order of magnitude lower than that of ST-R and similar to that

of the PH materials, the diffusivity of which is closely related to the fine Cu precipitates [38]. Since the additively manufactured materials (AM-x and AM-z) and ST-R were not subjected to the PH treatment, the difference in diffusivity values between the additively manufactured material and ST-R is attributed to another mechanism.

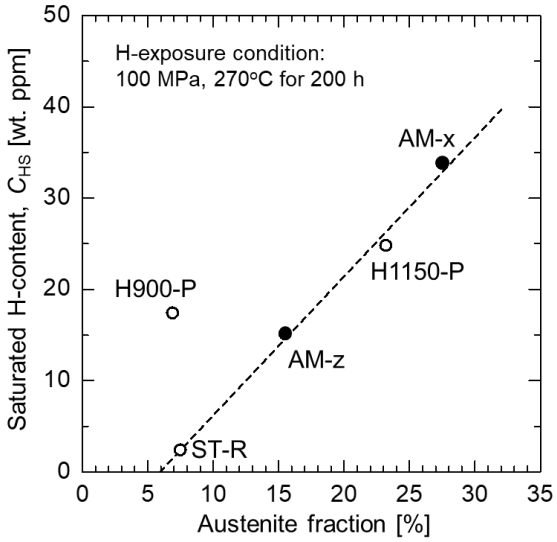

Fig. 7 Relationship between the saturated hydrogen content and austenite fraction of additively manufactured and conventional materials.

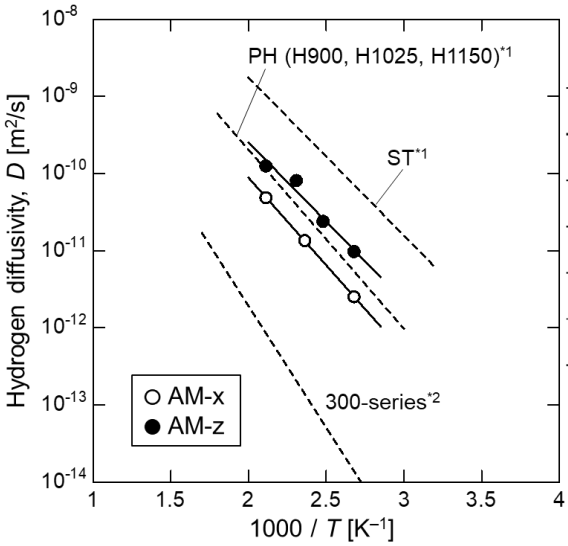

$$D = D_0 \exp\left(-\frac{E_D}{RT}\right)$$

Symbol	D_0 [m²/s]	E_D [kJ/mol]
AM-x	3.06×10^{-6}	43.5
AM-z	3.24×10^{-6}	39.3
ST	2.20×10^{-5}	39.2
PH	9.01×10^{-6}	44.5
300-series	3.91×10^{-6}	60.4

*1) Yamabe et al., Mater Sci Eng A (2021)
*2) Yamabe et al., Int J Hydrogen Energy (2017)

Fig. 8 Arrhenius plots of AM-x and AM-z hydrogen diffusivity, together with literature data [12,38].

Figure 9 shows the relationship between the diffusivity at 150°C, D_{150}, and the austenite fraction of AM-x, AM-z, and ST-R. Based on the determined hydrogen diffusivities, the diffusivities at 150°C

are shown in **Fig. 9**. Regardless of the material types, the hydrogen diffusivity became higher with a decrease in the austenite fraction, suggesting that the lower hydrogen diffusivities of AM-x and AM-z compared to that of ST-R were mainly attributed to their different austenite fractions. A similar tendency was observed from the hydrogen diffusivity of a cold-rolled Type 304 steel [47].

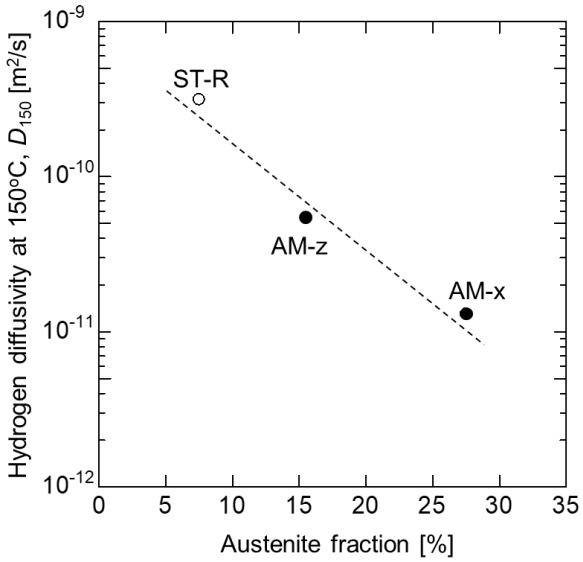

Fig. 9 Relationship between hydrogen diffusivity and austenite fraction.

3.5 Tensile properties

3.5.1 Uncharged additively manufactured materials

Figure 10 shows the nominal (engineering) stress and stroke relationships of the uncharged and H-charged specimens of AM-x and AM-z. Tests of AM-x and AM-z were conducted twice for the H-charged specimens, and the values of reduction in area (RA) and relative RA (RRA) are also indicated in the figure. Nominal strains were conveniently calculated by dividing the stroke by the gage length, enabling a comparison with the results in **Fig. 11**. **Figure 11** shows the nominal stress and strain relationships of the uncharged and H-charged specimens of ST-R, H900-R, H1025-R, and H1150-R, most of which were obtained from Ref. [38]. The ST treatment of H1025-R was implemented at 1040°C for 1 h, followed by water-quenching and the PH treatment was introduced at 550°C, followed by air-cooling. For the rectangular specimens, whereas the uncharged specimens failed after reaching the maximum stress, which means tensile strength (TS), accompanied by nonuniform deformation, the H-charged specimens failed before reaching the maximum stress. For the round-bar specimen, the uncharged and H-charged specimens except for H900-R exposed to 100 MPa H_2 gas failed after the maximum stress. The hydrogen effect on the tensile ductility is discussed in Section **3.5.2**; the tensile ductility of the uncharged specimens is discussed here.

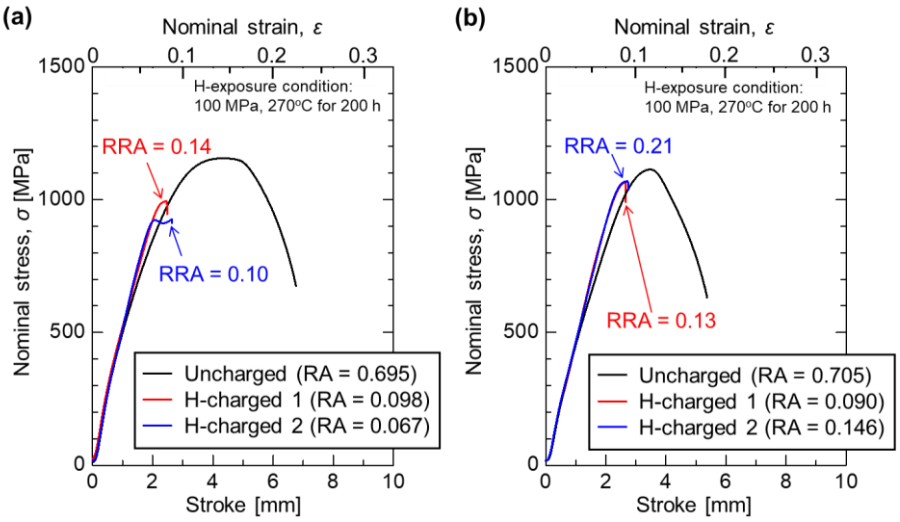

Fig. 10 Nominal stress and stroke curves of uncharged and H-charged rectangular specimens of AM-x (a) and AM-z (b).

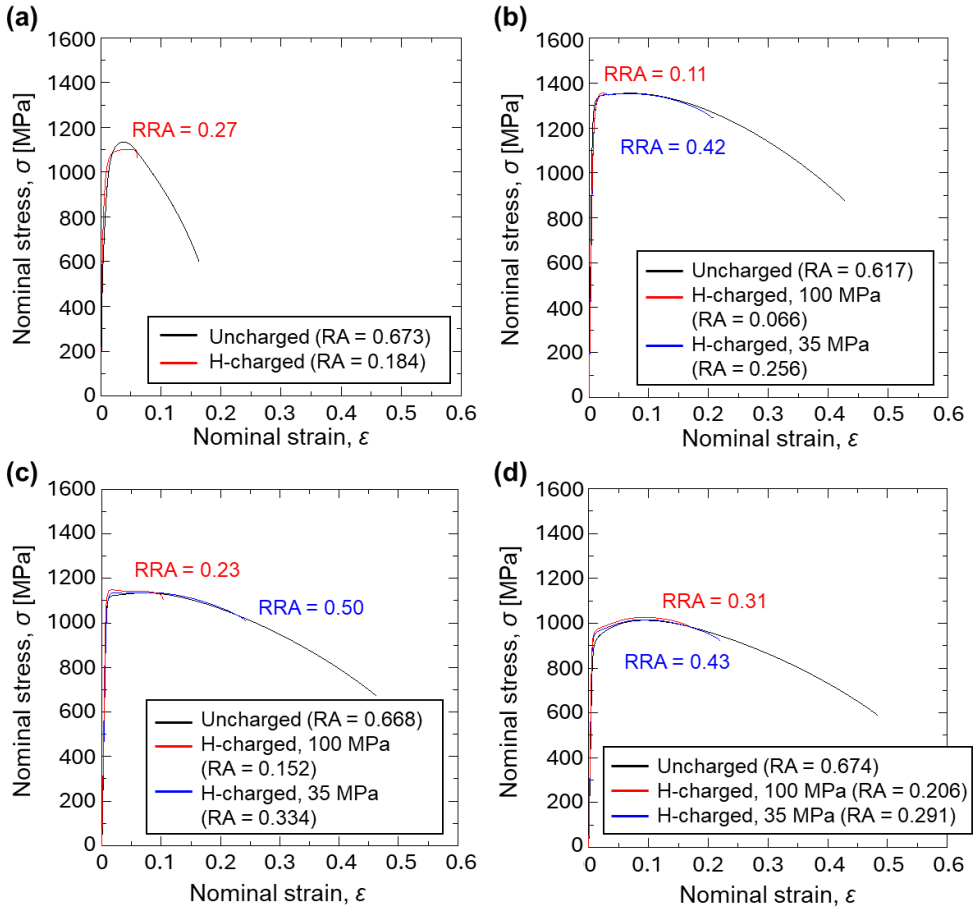

Fig. 11 Nominal stress and strain curves of uncharged and H-charged round-bar specimens of ST-R (a), H900-R (b), H1025-R (c), and H1150-R (d) [38].

Figures 12(a) compares the RA values for the uncharged specimens of AM-x and AM-z with those for various conventional materials. The TS and RA of ST-R were 1134 MPa and 0.673, respectively. Whereas the TS of ST-R was similar to that of AM-x and AM-z, the RA of ST-R was slightly lower than that of AM-x and AM-z. The RA values for AM-x and AM-z were also equal to or higher than those of the conventional materials. Compared with conventional materials, additively manufactured materials have been reported to generally show a higher tensile strength because of the fine microstructures and lower ductility resulting from the existence of porosities [39]. However, the porosity fraction of AM-x and AM-z was nearly zero, as known from **Fig. 4**; therefore, the RA values of the additively manufactured materials were considered to be not affected by such porosities.

3.5.2 H-charged additively manufactured materials

As understood from **Fig. 10**, the ductility of AM-x and AM-z was degraded by hydrogen. **Figure 12(b)** the RA values for the H-charged specimens of AM-x and AM-z with those for various conventional materials. The detailed of this figure will be discussed in Section **4.2**. **Figure 12(c)** compares the RRA values of AM-x and AM-z with those of various conventional materials [38]. The average RRA of AM-x was lower than that of AM-z. In general, the RRA became lower with an increase in TS. The RRA values of the conventional materials showed such a tendency, regardless of the heat-treatment conditions. Focusing on AM-x and AM-z, these RRA values were lower than those of ST-R and H1025-R with a TS value similar to that of AM-x and AM-z; the ductility loss of the additively manufactured materials was more significant than that of the conventional materials.

3.6 Fracture morphologies

3.6.1 Uncharged materials

Figure 13(a) shows low-magnified SEM images of the uncharged and H-charged specimens of the additively manufactured materials. The fracture surfaces consisted of the normal stress fracture region at the center and the shear stress fracture region near the surface, representing an ordinary cup and cone fracture. **Figure 13(b)** shows the high-magnified SEM images of AM-x, AM-z, and ST-R. Although the fracture surfaces on the normal stress fracture region of both the additively manufactured and conventional materials were covered with dimples, the size and number of the voids in the additively manufactured materials were smaller and larger, respectively, than those in the conventional materials. As shown in **Fig. 5**, the microstructure of the additively manufactured materials was finer than that of the conventional materials and is therefore deemed to be related to the void size.

3.6.2 H-charged materials

Regarding the H-charged specimens, unlike the uncharged specimens, the shear stress fracture region was observed only at one part near the specimen surface. From the nominal stress and stroke

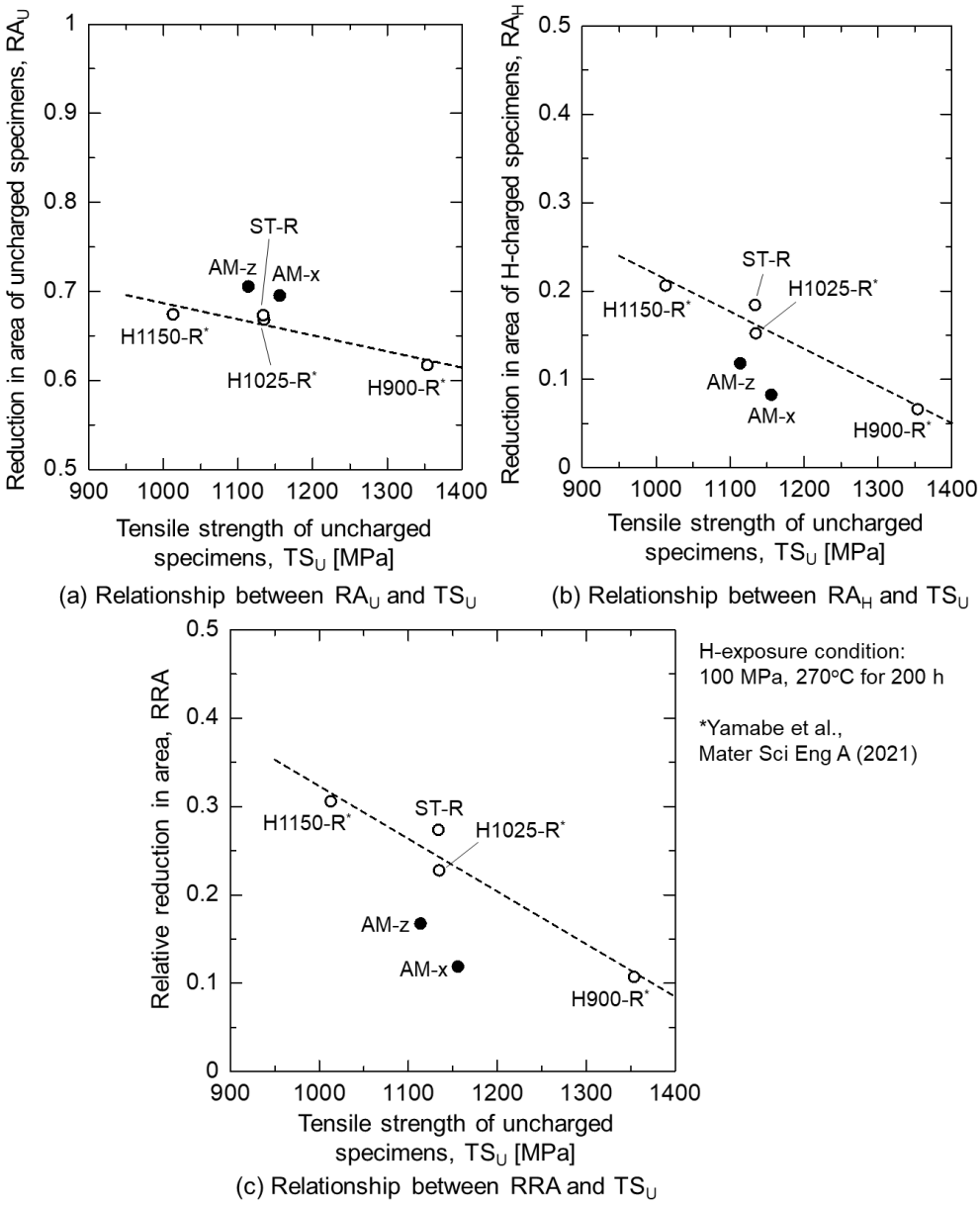

Fig. 12 Relationship between RA, RRA, and TS of uncharged and H-charged, additively manufactured and conventional materials [38].

relationships in **Fig. 10**, the H-charged specimens failed before reaching the maximum stress; therefore, we considered that the fracture occurred by a different mechanism from the formation and growth of voids due to triaxial stress. **Figures 13(a-1-3)** and **13(a-2-3)** show the side surfaces of the uncharged and H-charged specimens of AM-x. The observations were conducted from the directions shown by the arrows in **Figs. 13(a-1-1)** and **13(a-2-1)**. Many surface cracks were observed only in the H-charged specimen. Since there was no hydrogen at the surface of the H-charged specimen, these cracks were

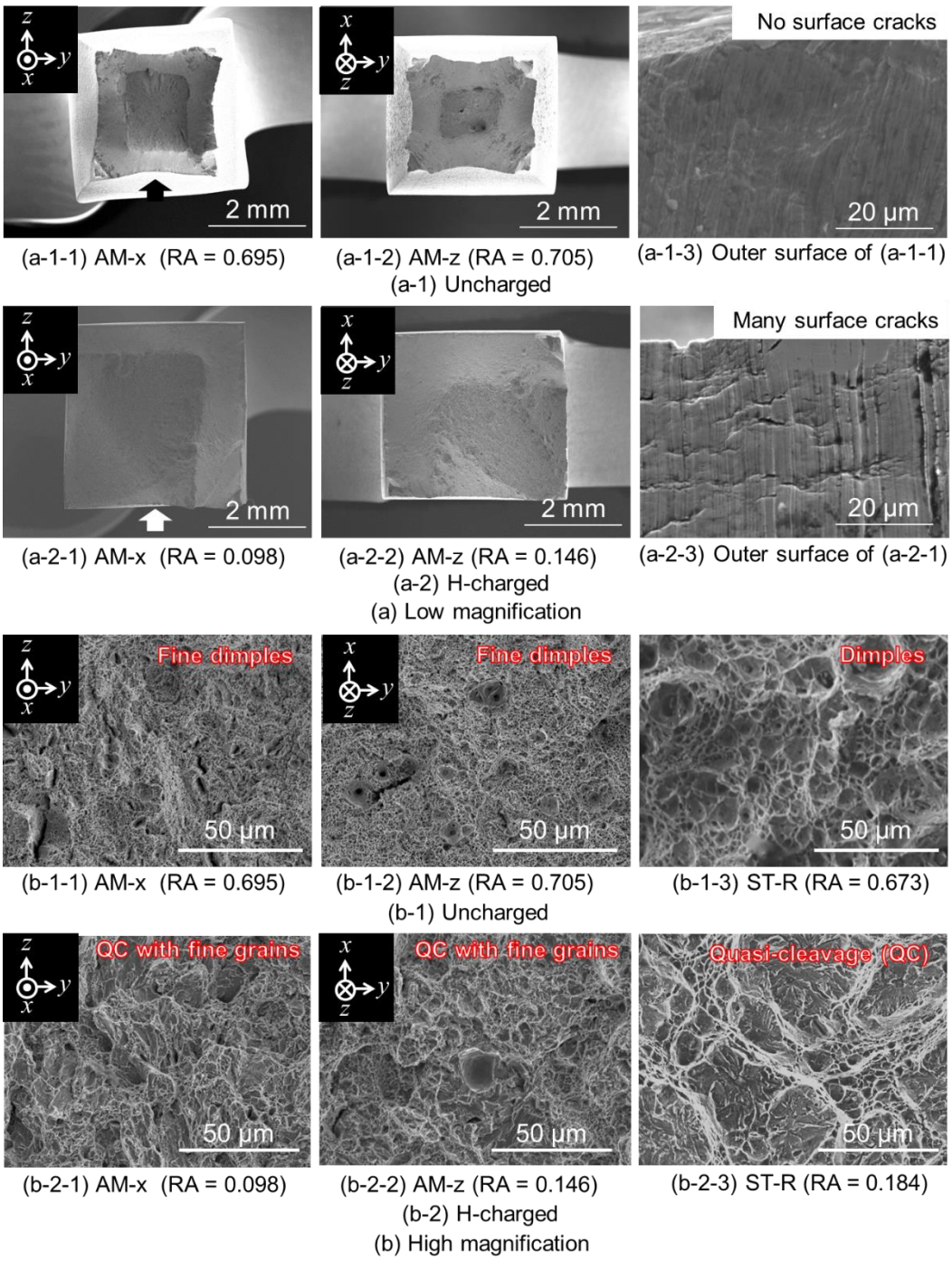

Fig. 13 Fracture surface morphologies and crack initiation behaviors of outer surfaces of uncharged and H-charged, additively manufactured (AM-x, AM-z), and conventional (ST-R) materials at (a) low magnification and (b) high magnification.

deemed to originate from the interior of the specimen and eventually reach the surface. According to our previous study [38], the fracture surface of H900-R was mainly covered with cleavage (C) facets, but that of H1150-R was covered with a mixture of quasi-cleavage (QC) and intergranular (IG) facets.

In the present study, the fracture surfaces of AM-x, AM-z, and ST-R were covered with QC facets and no C or IG facets were detected from these materials.

4. Discussion

4.1 Possible mechanism of HE for additively manufactured material

The crack growth behavior of the conventional materials with PH treatment (H900 and H1150) was observed in detail in our previous study [38]. The effects of the hydrogen content and TS on the fracture surface morphologies of the materials were investigated using H-charged specimens exposed to hydrogen gas under various hydrogen gas pressures, resulting in the detection of an H-induced C fracture and H-induced IG fracture in H900-R and H1150-R, respectively. These fracture morphologies were also observed in cryogenic impact tests where hydrogen–dislocation interactions were minor; therefore, the previous study concluded that these morphologies were mainly attributed to the hydrogen-enhanced decohesion (HEDE) mechanism [48,49]. The reason why the H-induced IG fracture occurred in H1150-R is considered to be related to a reduced IG strength due to hydrogen trapped at the IG precipitates. On the other hand, the IG precipitates were hardly detected and a large amount of hydrogen was present in H900-R (~10 wt.ppm [38]) compared with Cr–Mo steels (~1 wt.ppm [45]). The lattice hydrogen content of a BCC iron at 100 MPa and 25°C was around 0.01 wt.ppm [50] and the hydrogen content of H900-R was 10^3 times larger than this lattice hydrogen content. These situations are deemed to cause the H-induced C fracture of H900-R, although this fracture is rare in martensite steels compared to the H-induced IG fracture.

Although the fracture surfaces of AM-x and AM-z were finer than that of ST-R, they were fully covered with QC facets, which were also observed in some parts of the fracture surfaces of the H-charged specimen of H1150-R [38]. **Figure 14** shows the longitudinal cross sections of the uncharged and H-charged specimens of AM-x. The longitudinal cross section of the H-charged specimen of H1150-R was used as a reference. In AM-x, the voids of the uncharged specimen were elongated in the direction parallel to the loading direction, whereas the voids of the H-charged specimen were elongated in the direction perpendicular to the loading direction. This void growth behavior of the H-charged specimen was also observed in the H-charged specimen of H1150-R. As shown in **Fig. 14(d)**, the void of the H-charged specimen of AM-x grew in grains surrounded by martensite, which corresponded to the QC facets (**Fig. 13(b-2-3)**). In the case of H1150-R, the voids of the H-charged specimen grew in grains and near grain boundaries, as shown in **Fig. 14(e)**, which corresponded to the QC or IG facets, respectively. Voids elongated in the direction perpendicular to the loading direction have been observed in a H-charged carbon steel [51,52]. In those studies [51,52], the voids grew at a smaller plastic strain than that needed for the uncharged specimen. In addition, localized plastic deformation by hydrogen enhanced the growth and coalescence of the voids [53,54]. More detailed observations were conducted for QC facets produced in martensite steels, revealing that the localized

slip deformation by hydrogen formed cracks along the slip planes in laths and cracks as a result of dislocation pile-ups in lath and block boundaries, leading to the formation of QC facets [55,56]. These observations suggest that hydrogen–dislocation interactions played an important role in the formation of the QC facets in AM-x, AM-z, and ST-R, although the size of the QC facets was not the same between these steels in relation to the fineness of the microstructures.

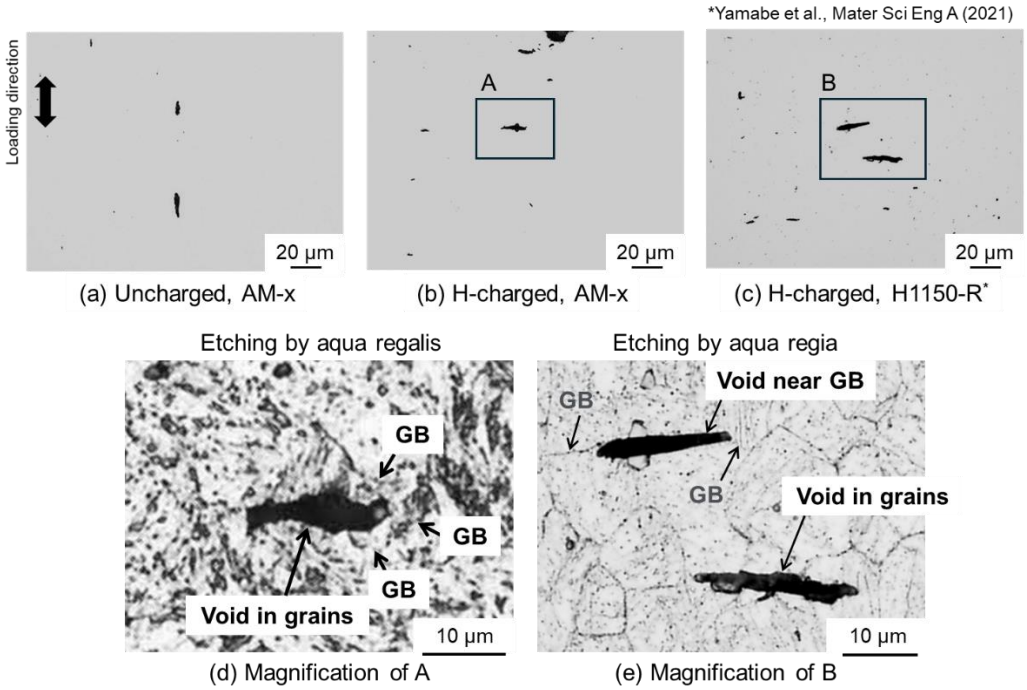

Fig. 14 Voids observed in longitudinal cross sections of uncharged and H-charged specimens of AM-x and a H-charged specimen of H1150-R.

4.2 Possible causes of the lower RAA of additively manufactured materials and RA in the presence of hydrogen

From the above discussion, the HE mechanism of AM-x and AM-z is considered to be the same as that of ST-R. In this section, possible causes for the lower RAA of additively manufactured materials are discussed. **Figure 15** represents the relationship between the RRA and austenite fraction of AM-x, AM-z, and ST-R. Although the RRA value decreased with an increase in the saturated hydrogen content, the saturated hydrogen content was related to the austenite fraction; as a result, the RRA value also decreased with a decrease in the austenite fraction. This observation implies that higher austenite phases and hydrogen contents of the additively manufactured materials are possible causes. In the presence of hydrogen, the steels containing metastable austenite phases show a remarkable degradation by hydrogen. In the case of solution-treated austenitic stainless steels, the RRA values are closely related to nickel-equivalent values as an indicator of austenite stability, being lower than a smaller nickel-equivalent

value [12,14]. As shown in **Fig. 14(d)**, the void of the H-charged specimen of AM-x was surrounded by martensite. Furthermore, additional XRD analysis was performed and then, the austenite fractions for the uncharged specimen of AM-x after the SSRT test were 4% at the uniform deformation region and zero at the local deformation region near the fracture surface, indicating that the austenite phases of the additively manufactured materials were metastable as reported in existing literatures [39–41]. These experimental results suggest that strain-induced martensite transformations of austenite containing a large amount of hydrogen occurred around voids during tensile deformation and then, caused a supersaturated hydrogen condition in the martensite, leading to the H-induced ductility loss. Regarding the higher hydrogen contents, as shown in **Fig. 11**, the ductility loss of H900-R, H1025-R, and H1150-R was evaluated using the specimens with different hydrogen contents, revealing that the RRA values decreased with increasing hydrogen content. Because the hydrogen contents of AM-x and AM-z were greater than that of ST, these higher hydrogen contents might have enhanced the lower RRA of the additively manufactured material.

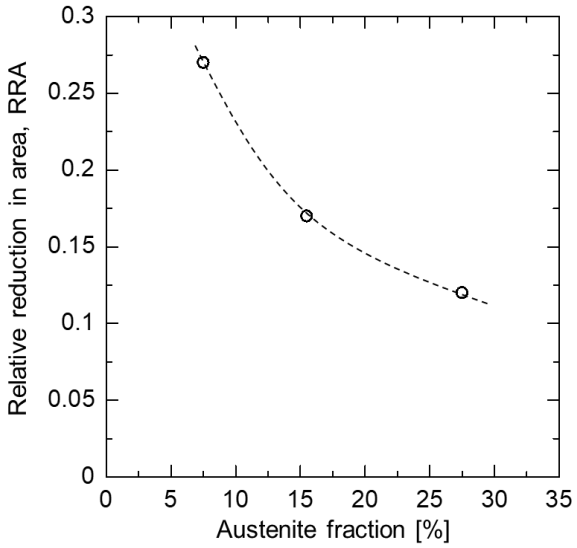

Fig. 15 Relationship between RRA and austenite fraction of AM-x, AM-z, and ST-R.

Finally, we used a relative property such as RRA to determine the degree of HE; however, it is important to also consider the absolute property from a performance/design perspective. As shown in **Fig. 12(b)**, RA_H, of AM-x and AM-z with those for various conventional materials. Although the RA_H values of AM-x and AM-z were lower than those of ST and H1025-R with similar TS values, the differences became smaller than in the case of the comparison based on RRA because the RA_U values of the additively manufactured materials were greater than those of the conventional ones. If even higher RA_U values of the additively manufactured materials are attained to optimize manufacturing parameters, the RA_H values might be greater than those of ST and H1025-R, despite their lower RRA

values. In this situation, the additively manufactured materials would be better suited for hydrogen service, suggesting that the absolute property warrants the same attention as the relative property.

4. Conclusions

To acquire fundamental data for discussing the hydrogen compatibility of materials, this study investigated the hydrogen diffusion properties and hydrogen-induced ductility loss of a precipitation-hardened martensitic stainless steel (17-4PH) produced by additive manufacturing (AM). The results obtained from the additively manufactured materials with as-built conditions were compared with those of conventional materials, namely solution-treated (ST) and precipitation-hardened (H900, H1150) specimens of conventional 17-4PH steels. The conclusions are summarized as follows:

1. The austenite fractions of the additively manufactured materials were at most three times higher than that of the ST material.
2. Except for H900, the saturated hydrogen content of the additively manufactured and conventional materials became larger with an increase in the austenite fraction. The reason for the H900 exception is considered to be its saturated hydrogen content that was dominated by hydrogen trapping by fine Cu precipitates.
3. For both the additively manufactured and conventional materials, the hydrogen diffusivity was also closely related to the austenite fraction, showing that the diffusivity was lower with a higher austenite fraction.
4. The reduction in area (RA) of the uncharged additively manufactured materials was larger than that of the uncharged conventional ST and PH materials. Additionally, although the fracture surfaces of the additively manufactured and conventional materials were covered with dimples, the sizes of the voids in the additively manufactured materials were smaller than those in the conventional materials, suggesting a contribution of the fine microstructures of the additively manufactured materials.
5. When comparing the relative RA (RRA) values between the additively manufactured and conventional materials with similar tensile strength, the RRA of the additively manufactured materials was lower than that of the conventional materials, revealing that the hydrogen-induced ductility loss of the additively manufactured materials was more significant.
6. Although the fracture units differed between the additively manufactured and ST materials, their fracture surfaces were covered with quasi-cleavage (QC) facets. Voids elongated in the direction perpendicular to the loading direction corresponding with the QC facets were observed from longitudinal cross sections. Similar voids were observed in other steels and were considered to be formed in relation to localized slip deformations enhanced by hydrogen.
7. Although the RRA value of the additively manufactured and ST materials decreased with increasing saturated hydrogen content, the saturated hydrogen content was also related to the

austenite fraction. Therefore, higher hydrogen contents and austenite phases of the additively manufactured materials are inferred to be possible causes of the lower RAA of the additively manufactured materials.

CRediT authorship contribution statement

Junichiro Yamabe: Conceptualization; Methodology; Investigation; Supervision; Writing - Original Draft; Soma Kato: Investigation; Visualization; Kazuyuki Morishita: Resources; Validation; Writing - Review & Editing; Kentaro Wada: Investigation; Validation; Writing - Review & Editing

Declaration of competing interest

The authors declare that they have no known competing financial interests or personal relationships that could have appeared to influence the work reported in this paper.

References

[1] Han G, He J, Fukuyama S, Yokogawa K. Effect of strain-induced martensite on hydrogen environment embrittlement of sensitized austenitic stainless steels at low temperature. Acta Metall 1998;46:4559–70. https://doi.org/10.1016/S1359-6454(98)00136-0

[2] Fukuyama S, Sun D, Zhang L, Wen M, Yokokawa K. Effect of temperature on hydrogen environment embrittlement of type 316 series austenitic stainless steels at low temperature. J Jpn Inst Met 2003;9:456–9. https://doi.org/10.2320/jinstmet1952.67.9_456

[3] San Marchi C, Somerday BP, Tang X, Schiroky GH. Effects of alloy composition and strain hardening on tensile fracture of hydrogen-precharged type 316 stainless steels. Int J Hydrogen Energy 2008;33:889–904. https://doi.org/10.1016/j.ijhydene.2007.10.046

[4] Michler T, Nauman J. Hydrogen environment embrittlement of austenitic stainless steels at low temperature. Int J Hydrogen Energy 2008;33:2111–22. https://doi.org/10.1016/j.ijhydene.2008.02.021

[5] Michler T, Yukhimchuk AA, Naumann J. Hydrogen environment embrittlement testing at low temperatures and high pressures. Corros Sci 2008;50:3519–26. https://doi.org/10.1016/j.corsci.2008.09.025

[6] San Marchi C, Michler T, Nibur KA, Somerday BP. On the physical differences between tensile testing of type 304 and 316 austenitic stainless steels with internal hydrogen and in external hydrogen. Int J Hydrogen Energy 2010;35:9736–45. https://doi.org/10.1016/j.ijhydene.2010.06.018

[7] Mine Y, Kimoto T. Hydrogen uptake in austenitic stainless steels by exposure to gaseous hydrogen and its effect on tensile deformation. Corros Sci 2011;53:2619–29. https://doi.org/10.1016/j.corsci.2011.04.022

[8] Michler T, San Marchi C, Naumann J, Weber S. Hydrogen environment embrittlement of stable austenitic steels. Int J Hydrogen Energy 2012;37:6231–46. https://doi.org/10.1016/j.ijhydene.2012.08.071

[9] Yamabe J, Matsuoka S, Murakami Y. Surface coating with a high resistance to hydrogen entry under high-pressure hydrogen-gas environment. Int J Hydrogen Energy 2013;38:10141–54. https://doi.org/10.1016/j.ijhydene.2013.05.152

[10] Matsuo T, Yamabe J, Matsuoka S. Effects of hydrogen on tensile properties and fracture surface morphologies of Type 316L stainless steel. Int J Hydrogen Energy 2014;39:3542–51. https://doi.org/10.1016/j.ijhydene.2013.12.099

[11] Matsuoka S, Yamabe J, Matsunaga H. Criteria for determining hydrogen compatibility and the mechanisms for hydrogen-assisted surface crack growth in austenitic stainless steels. Eng Fract Mech 2016;153:103–27. https://doi.org/10.1016/j.engfracmech.2015.12.023

[12] Yamabe J, Takakuwa O, Matsunaga H, Itoga H, Matsuoka S. Hydrogen diffusivity and tensile-ductility loss of solution-treated austenitic stainless steels with external and internal hydrogen. Int J Hydrogen Energy 42;2017:13289–99. https://doi.org/10.1016/j.ijhydene.2017.04.055

[13] Takakuwa O, Yamabe J, Matsunaga H, Matsuoka S. Comprehensive understanding of ductility loss mechanisms in various steels with external and internal hydrogen. Metall Mater Trans A 2017;48:5717–32. https://doi.org/10.1007/s11661-017-4323-3

[14] Kobayashi H, Yamada T, Kobayashi H, Matsuoka S. Criteria for selecting materials to be used for hydrogen refueling station equipment. ASME PVP2016-64033; 2016. https://doi.org/10.1115/PVP2016-64033

[15] Hirayama T, Ogirima M. Influence of chemical composition on martensitic transformation in Fe-Cr-Ni stainless steel. J Jpn Inst Met 1970;34:507–10. https://doi.org/10.2320/jinstmet1952.34.5_507

[16] Takaki S, Namba S, Imakawa K, Macadre A, Yamabe J, Matsunaga H, Matsuoka S. Determination of hydrogen compatibility for solution-treated austenitic stainless steels based on a newly proposed nickel-equivalent equation. Int J Hydrogen Energy 2016;41:15095–100. https://doi.org/10.1016/j.ijhydene.2016.06.193

[17] San Marchi C, Somerday BP, Nibur KA. Development of Methods for Evaluating Hydrogen Compatibility and Suitability. Int J Hydrogen Energy 2014;39:20434–9. https://doi.org/10.1016/j.ijhydene.2014.03.234

[18] San Marchi C, Yamabe J, Schwarz M, Matsunaga H, Zickler S, Matsuoka S, Kobayashi H. Global Harmonization of Fatigue Life Testing in Gaseous Hydrogen. ASME PVP2018-84898; 2018. https://doi.org/10.1115/PVP2018-84898

[19] Yamabe J, Matsunaga H, Furuya Y, Hamada S, Itoga H, Yoshikawa M, Takeuchi E, Matsuoka S. Qualification of chromium–molybdenum steel based on the safety factor multiplier method

in CHMC1-2014. Int J Hydrogen Energy 2015;40:719–28. https://doi.org/10.1016/j.ijhydene.2014.10.114

[20] Matsuoka S, Yamabe J, Matsunaga H. Criteria for determining hydrogen compatibility and the mechanisms for hydrogen-assisted surface crack growth in austenitic stainless steels. Eng Fract Mech 2016;153:103–27. https://doi.org/10.1016/j.engfracmech.2015.12.023

[21] Yamabe J, Itoga H, Awane T, Matsuo T, Matsunaga H, Matsuoka S. Pressure cycle testing of Cr-Mo steel pressure vessels subjected to gaseous hydrogen. J Pres Ves Technol 2016;138:011401. https://doi.org/10.1115/1.4030086

[22] Seifi M, Gorelik M, Waller J, Hrabe N, Daniewicz S, Lewandowski J.J. Progress towards metal additive manufacturing standardization to support qualification and certification. JOM 2017;69:439–55. https://doi.org/10.1007/s11837-017-2265-2

[23] Egashira K, Furumoto T, Hishida K, Abe S, Koyano T, Hashimoto Y, Hosokawa A. Formation mechanism of pores inside structure fabricated by metal-based additive manufacturing. Int J Automation Technol 2019;13:330–7. https://doi.org/10.20965/ijat.2019.p0330

[24] Panchenko M, Melnikov E, Moskvina V, Astafurov S, Maier G, Reunova K, Rubtsov V, Kolubaev E, Astafurova E. The effect of hydrogen-charging on mechanical properties of austenitic CrNi steel fabricated by wire-feed electron beam additive manufacturing. E3S Web of Conferences 2021;225:2020–2022. https://doi.org/10.1051/e3sconf/202122501011

[25] Pham MS, Dovgyy B, Hooper PA. Twinning induced plasticity in austenitic stainless steel 316L made by additive manufacturing. Mater Sci Eng A 2017;704:102–11.

[26] Smith, TR, San Marchi C, Sugar JD, Balch DK. Effects of extreme hydrogen environments on the fracture and fatigue behavior of additively manufactured stainless steels. ASME PVP 2019-93903;2019. https://doi.org/10.1115/PVP2019-93903

[27] Yin YJ, Sun JQ, Guo J, Kan XF, Yang DC. Mechanism of high yield strength and yield ratio of 316 L stainless steel by additive manufacturing. Mater Sci Eng A 2019;744:773–7. https://doi.org/10.1016/j.msea.2018.12.092

[28] Wang YM, Voisin T, Mckeown JT, Ye J, Calta NP, Li Z, Zeng Z, Zhang Y, Chen W, Roehling TT, Ott RT, Santala MK, Depond PJ, Matthews MJ, Hamza AV, Zhu T. Additively manufactured hierarchical stainless steels with high strength and ductility. Nat Mater 2018;17:63–70. https://doi.org/10.1038/nmat5021

[29] Silverstein R, Eliezer D. Hydrogen trapping in 3D-printed (additive manufactured) Ti-6Al-4V. Mater Charact 2018;144:297–304. https://doi.org/10.1016/j.matchar.2018.07.029

[30] Zou Z, Simonelli M, Katrib J, Dimitrakis G, Hague R. Microstructure and tensile properties of additive manufactured Ti-6Al-4V with refined prior-β grain structure obtained by rapid heat treatment. Mater Sci Eng A 2021;814:141271. https://doi.org/10.1016/j.msea.2021.141271

[31] Xiao H, Li S, Han X, Mazumder J, Song L. Laves phase control of Inconel 718 alloy using quasi-continuous-wave laser additive manufacturing. Mater Des 2017;122:330–9. https://doi.org/10.1016/j.matdes.2017.03.004

[32] Hirayama A, Kimura M, Kusano M, Kaizu K. Microstructure and mechanical properties of AlSi12CuNi alloy fabricated by laser powder bed fusion process. Int J Automation Technol 2021;15:388–95. https://doi.org/10.20965/ijat.2021.p0388

[33] Barkia B, Aubry P, Haghi-Ashtiani P, Auger T, Gosmain L, Shuster F, Maskrot H. On the origin of the high tensile strength and ductility of additively manufactured 316L stainless steel: Multiscale investigation. J Mater Sci Technol 2020;41:209–18. https://doi.org/10.1016/j.jmst.2019.09.017

[34] Bertsch KM, Nagao A, Rankouhi B, Kuehl B, Thoma DJ. Hydrogen embrittlement of additively manufactured austenitic stainless steel 316 L. Corros Sci 2021;192:109790. https://doi.org/10.1016/j.corsci.2021.109790

[35] He J, Liu Q, He M, Li J, Wang S. The hydrogen embrittlement of pure Ni fabricated by additive manufacturing. Int J Hydrogen Energy 2023;48:16910–22. https://doi.org/10.1016/j.ijhydene.2023.01.167

[36] Baek S-W, Song EJ, Kim JH, Jung M, Baek UB, Nahm SH. Hydrogen embrittlement of 3-D printing manufactured austenitic stainless steel part for hydrogen service. Scr Mater 2017;130:87–90. https://doi.org/10.1016/j.scriptamat.2016.11.020

[37] Lee D-H, Sun B, Lee S, Ponge D, Jägle EA, Raabe D. Comparative study of hydrogen embrittlement resistance between additively and conventionally manufactured 304L austenitic stainless steels. Mater Sci Eng A 2021;803:140499. https://doi.org/10.1016/j.msea.2020.140499

[38] Yamabe J, Sezgin J-G, Wada K. Interpretation of complex, tensile-fracture phenomena in precipitation-hardened, martensitic stainless steels, 17-4PH, in presence of hydrogen. Mater Sci Eng A 2021;823:141717. https://doi.org/10.1016/j.msea.2021.141717

[39] Haghdadi N, Laleh M, Moyle M, Primig S. Additive manufacturing of steels; a review of achievements and challenges. J Mater Sci 2021;56:64–107. https://doi.org/10.1007/s10853-020-05109-0

[40] LeBrun T, Tanigaki K, Horikawa K, Kobayashi H. Strain rate sensitivity and mechanical anisotropy of selective laser melted 17-4 PH stainless steel. Mech Eng J 2014;1:1–13. https://doi.org/10.1299/mej.2014smm0049

[41] LeBrun T, Nakamoto T, Hirokawa K, Kobayashi H. Effect of retained austenite on subsequent thermal processing and resultant mechanical properties of selective larger melted 17-4 PH stainless steel. Mater Des 2015;81:44–53. https://doi.org/10.1016/j.matdes.2015.05.026

[42] Alnajjar M, Christien F, Bosch C, Wolski K. A comparative study of microstructure and hydrogen embrittlement of selective laser melted and wrought 17-4 PH stainless steel. Mater Sci Eng A 2020;785:139363. https://doi.org/10.1016/j.msea.2020.139363

[43] Demarez A, Hock AG, Meunier FA. Diffusion of hydrogen in mild steel. Acta Metall 1954;2:214–23. https://doi.org/10.1016/0001-6160(54)90162-5

[44] Matsuo T, Yamabe J, Furukawa H, Seki K, Shimizu K, Watanabe S, Matsuoka S. Development of New Strain Gage for High-Pressure Hydrogen Gas Use. Exp Mech 2014;54:431–42. https://doi.org/10.1007/s11340-013-9816-4

[45] Yamabe J, Awane T, Matsuoka S. Investigation of hydrogen transport behavior of various low-alloy steels with high-pressure hydrogen gas. Int J Hydrogen Energy 2015;40:11075–86. https://doi.org/10.1016/j.ijhydene.2015.07.006

[46] Isobe S, Okabe M. Kinetics of reverted austenite formation and its effects on the properties of 17-4PH stainless steel. DENKI-SEIKO 1983;54:253–64. https://doi.org/10.4262/denkiseiko.54.253

[47] Sezgin J-G, Takatori D, Yamabe J. Anisotropy of cold-worked Type-304 austenitic stainless steel: focus on the hydrogen diffusivity. Int J Hydrogen Energy 2019;44:20516–28. https://doi.org/10.1016/j.ijhydene.2019.05.175

[48] Pfeil LB. The effect of occluded hydrogen on the tensile strength of iron. Proc R Soc A Math Phys Eng Sci 1926;112:185–95. https://doi.org/10.1098/rspa.1926.0103

[49] Troiano AR. The role of hydrogen and other interstitials in the mechanical behavior of metals. Metallogr Microstruct Anal 2016;5:557–69. https://doi.org/10.1007/s13632-016-0319-4

[50] Hirth JP. Effects of hydrogen on the properties of iron and steel. Metall Trans A 1980;11:861–90. https://doi.org/10.1007/BF02654700

[51] Matsuo T, Honma N, Matsuoka S, Murakami Y. Effect of hydrogen and prestrain on tensile properties of carbon steel SGP (0.078 C-0.012 S-0.35 Mn, mass%) for 0.1 MPa hydrogen pipeline. Trans JSME A 2008;74:1164–73. https://doi.org/10.1299/kikaia.74.1164

[52] Murakami Y, Matsuoka S. Effect of hydrogen on fatigue crack growth of metals. Eng Fract Mech 2010;77:1926–40. https://doi.org/10.1016/j.engfracmech.2010.04.012

[53] Beachem CD. A new model for hydrogen-assisted cracking (hydrogen "embrittlement"). Metall Trans 1972;3:441–55. https://doi.org/10.1007/BF02642048

[54] Birnbaum HK, Sofronis P. Hydrogen-enhanced localized plasticity—a mechanism for hydrogen-related fracture. Mater Sci Eng A 1994;176:191–202. https://doi.org/10.1016/0921-5093(94)90975-X

[55] Shibata A, Takahashi H, Tsuji N. Microstructural and crystallographic features of hydrogen-related crack propagation in low carbon martensitic steel. ISIJ Int 2012;52:208–12. https://doi.org/10.2355/isijinternational.52.208

[56] Nagao A, Dadfarnia M, Somerday BP, Sofronis P, Ritchie RO. Hydrogen-enhanced-plasticity mediated decohesion for hydrogen-induced intergranular and “quasi-cleavage” fracture of lath martensitic steels. J Mech Phys Sol 2018;112:403–30. https://doi.org/10.1016/j.jmps.2017.12.016